ORIGINAL PAPER

Magnetic Chitosan-Glutaraldehyde/Zinc Oxide/Fe$_3$O$_4$ Nanocomposite: Optimization and Adsorptive Mechanism of Remazol Brilliant Blue R Dye Removal

Abdallah Reghioua[1,2,3] · Djamel Barkat[1] · Ali H. Jawad[2] · Ahmed Saud Abdulhameed[4] · S. Rangabhashiyam[5] · Mohammad Rizwan Khan[6] · Zeid A. ALOthman[6]

Abstract

A magnetic Schiff's base chitosan-glutaraldehyde/Fe$_3$O$_4$ composite (CHT-GLA/ZnO/Fe$_3$O$_4$) was developed by incorporating zinc oxide (ZnO) nanoparticles into its structure to prepare an efficient adsorbent for the removal of remazol brilliant blue R (RBBR) dye. The CHT-GLA/ZnO/Fe$_3$O$_4$ was characterized by the following methods: CHN, BET, FTIR, XRD, SEM–EDX, pHpzc, and potentiometric titrations. Box-Behnken design based on response surface methodology was used to optimize the effects of the A: ZnO nanoparticles loading (0–50%), B: dose (0.02–0.1 g), C: pH (4–10), D: temperature (30–60 °C), and time E: (10–60 min) on the synthesis of the magnetic adsorbent and the RBBR dye adsorption. The experimental data of kinetics followed the pseudo-second order model, while isotherms showed better fit to Freundlich and Temkin models. The maximum adsorption capacity of the target nanocomposite (CHT-GLA/Fe$_3$O$_4$ containing 25% ZnO or CHT-GLA/ZnO/Fe$_3$O$_4$-25) was reached of 176.6 mg/g at 60 °C. The adsorption mechanism of RBBR onto CHT-GLA/ZnO/Fe$_3$O$_4$ nanocomposite can be attributed to multi-interactions including electrostatic attractions, hydrogen bonding, Yoshida H-bonding, and n-π interactions. This study offers a promising hybrid nanobiomaterial adsorbent in environmental nanotechnology to separate and remove the contaminants such as organic dyes from wastewater.

Keywords Magnetic chitosan · Zinc oxide nanoparticles · Remazol brilliant blue R dye · Glutaraldehyde · Response surface methodology

✉ Ali H. Jawad
ali288@uitm.edu.my; ahjm72@gmail.com

1. Laboratory of Molecular Chemistry and Environment, University of Biskra, PO Box 145, Biskra 07000, Algeria

2. Faculty of Applied Sciences, Universiti Teknologi MARA, 40450 Shah Alam, Selangor, Malaysia

3. University of El Oued, Fac. Technology, 39000 El Oued, Algeria

4. Department of Medical Instrumentation Engineering, Al-Mansour University College, Baghdad, Iraq

5. Department of Biotechnology, School of Chemical and Biotechnology, SASTRA Deemed University, Thanjavur, Tamil Nadu 613401, India

6. Advanced Materials Research Chair, Chemistry Department, College of Science, King Saud University, Riyadh 11451, Saudi Arabia

Introduction

Synthetic dyes are widely used in many industrial activities including paper, plastics, textile, cosmetic, leather, and pharmaceutical, which generate massive volumes of wastewaters [1]. Discharging of the organic dyes directly into surface water can cause serious water pollution, i.e. reducing photosynthesis activity, disordering the ecological balance of aquatic systems, and toxic effects on biota [2]. Moreover, several dyes can cause a series of adverse effects on human health [3]. Remazol brilliant blue R (RBBR) dye is a typical reactive dye, which is extensively used in the industrial for synthesis of polymeric dyes [4]. RBBR is considered as recalcitrant organic pollutants, which can cause several health problems [5]. Therefore, the treatment of the effluents containing dyestuffs before being fluxed into water streams is environmentally important. Several methods have been documented for the treatment of the effluents containing dyestuffs such as adsorption [6], membrane separation [7],

photodegradation [8], and coagulation [9]. Adsorption is regarded as one of an effective and eco-friendly method due to its exceptional benefits such as operational ease, high regeneration, low-cost, high removal efficiency, and harmless of the treated water [10].

Chitosan (CHT) is a linear biopolymer, and it is one of the most efficient and environmentally friendly adsorbents applied in adsorption method for the adsorption of dyes [11]. CHT shows several outstanding properties such as high hydrophilicity, ease of modification, biodegradability, nontoxicity, and super absorbency [12]. It is characterized by availability a large number of amino and hydroxyl groups, making it an excellent adsorbent for the removal of pollutants such as dyes and heavy metals [13]. However, applying of CHT in adsorption technology is limited due to high swelling index, low chemical stability in acidic environment, weak mechanical strength, and low surface area [4, 14].

Various procedures have been applied to pass these hurdles and enhance the physical and chemical properties of CHT such as crosslinking reaction [15], functionalization by organic groups [16], composition with inorganic materials [17], and grafting with carbon materials [18, 19]. The crosslinking character is one of the most common procedures, which is commonly used to increase the stability of CHT in an acidic medium and to improve mechanical strength [20]. CHT crosslinked absorbent materials have been vastly used for removal of dyes from water [21]. Furthermore, the CHT-based nanocomposites have been attracted significant interest due to its outstanding properties such as specific surface area, chemical stability, adsorption capacity, and thermal stability [22]. Various inorganic nanomaterials such as copper oxide (CuO) [23], nickel oxide (NiO) [24], and zinc oxide (ZnO) [25] have been introduced in preparation CHT nanocomposites to improve and enrich its properties. Among these, ZnO nanoparticles is one of the interesting inorganic materials for the development of CHT-based adsorbents due to its exceptional properties such as biocompatibility, safe to use, inexpensive, high surface area, preferable adsorption capacity, antimicrobial activity, chemical stability, and photo activity [26].

Recently, CHT/ZnO nanocomposites have received great attention as a key material in many applications such as food packaging [27], wastewater treatment [28], antibacterial [29], and biosensor [30]. Currently, magnetic adsorbents are receiving great attention from researchers due to its easy collection from an aqueous solution by magnetic tool after adsorption process. In the same regard, magnetite (Fe_3O_4) is one of the most magnetic particles used in preparation of magnetic adsorbents for water remediation application owing to its small particle size, biodegradability, high surface area, and temperature stability [31]. In fact, modifying CHT with nano scale materials is an effective strategy to enhance the physical property, thermal stability, surface area, and surface functionality of CHT. Moreover, the chemical modification of CHT by dialdehyde crosslinking agent and formation of Schiff's base CHT's derivatives is another effective strategy to enhance the chemical stability, prevent high level of swelling in aqueous environment, and reduce leachability in acidic environment.

Therefore, the main aim of this study is to develop a chemically stable Schiff's bases derivate of magnetic chitosan-glutaraldehyde/Fe_3O_4 composite (CHT-GLA/ZnO/Fe_3O_4). To achieve this goal, zinc oxide (ZnO) nanoparticles was loaded into polymeric structure of CHT and followed by crosslinking step via Schiff's base reaction using glutaraldehyde to obtain an effective adsorbent of magnetic chitosan-glutaraldehyde/ZnO/Fe_3O_4 nanocomposite (CHT-GLA/ZnO/Fe_3O_4). The effectiveness of CHT-GLA/ZnO/Fe_3O_4 was tested for the removal of remazol brilliant blue R (RBBR) dye from aqueous environment. The effect of the ZnO nanoparticles loading, dose, pH, temperature, and time on the synthesis of the adsorbent and the RBBR dye adsorption were evaluated and optimized by Box-Behnken design (BBD). Additionally, several kinetic and isotherm models were used to describe the adsorption mechanism and to determine the adsorption capacity of the synthesized nanocomposite. Finally, a proposed adsorption mechanism for RBBR onto CHT-GLA/ZnO/Fe_3O_4 was discussed.

Materials and Methods

Materials

CHT ($\geq 75\%$ degree of deacetylation), ZnO nanopowder, GLA solution, and RBBR ($C_{22}H_{16}N_2Na_2O_{11}S_3$; MW: 626.54; g/mol $\lambda_{max} = 592$ nm) were supplied by Sigma–Aldrich. Iron (III) chloride hexahydrate ($FeCl_3.6H_2O$, MW: 270.30 g/mol), and Iron (II) chloride tetrahydrate ($FeCl_2.4H_2O$, MW:198.81 g/mol) were supplied from HmbG Chemicals and Bendosen Laboratory Chemicals, respectively. Acetic acid (CH_3COOH), sodium chloride (NaCl), hydrochloric acid (HCl), and sodium hydroxide (NaOH) were ordered from R&M Chemicals.

Synthesis of CHT-GLA/ZnO/Fe_3O_4

1 g of CHT flakes were poured in 60 mL of CH_3COOH acid solution (5% v/v) and agitated at 550 rpm on a magnetic stirrer for 24 h at 25 °C to dissolve CHT flakes. Subsequently, 10 mL aqueous solution of Fe^{3+}/Fe^{2+} ions (3.9 g $FeCl_3 \cdot 6H_2O$ and 2.7 g $FeCl_2 \cdot 4H_2O$) was added to CHT solution with stirring for 1 h. The magnetic CHT/Fe_3O_4 beads were obtained by dropping of the mixture solution as drops into 1000 mL of NaOH solution (2 M). The resulting magnetic CHT hydrogel beads were washed

with distilled water until become neutral. Cross-linking process of the magnetic beads was accomplished by adding them into flask containing 80 mL GLA (2%) with mild stirring in shaker bath incubator at 40 °C for 2 h. The resultant was washed and then dried at 60 °C overnight in oven to get the final CHT-GLA/Fe_3O_4 composite. For the purpose of comparison, chitosan-glutaraldehyde/ZnO/Fe_3O_4 nanocomposite was prepared by mixing different ratios (wt%) of ZnO nanoparticles with chitosan before adding to CH_3COOH solution, i.e. 25:75 wt% (ZnO:CHT), which was named as CHT-GLA/ZnO/Fe_3O_4-25 and 50:50. wt% (ZnO:CHT), which was named as CHT-GLA/ZnO/Fe_3O_4-50. Ultimately, the synthesized composites were pulverized and then sieved at a particle size (≤ 250 µm) for further use. Figure 1 demonstrates the fabrication steps of the CHT-GLA/ZnO/Fe_3O_4 nanocomposite.

Characterization

The specific surface area, and average pore width of the synthesized composites were analyzed by Brunauer–Emmett–Teller (BET) approach (Micromeritics ASAP 2060). The textural and morphological characteristics of the synthesized composites and target composite (CHT-GLA/ZnO/Fe_3O_4-25) after RBBR adsorption were observed by scanning electron microscope (SEM, Zeiss Supra 40 VP). The chemical qualitative analysis was also performed for the synthesized composites with energy dispersive X-Ray analysis (EDX). The phase determination of the synthesized composites was characterized by X–ray powder diffractometry (XRD, X'Pert PRO, PAnalytical). The surface chemical characteristics of the synthesized composites and the target composite (CHT-GLA/ZnO/Fe_3O_4-25) after RBBR adsorption were defined by Fourier Transforms infrared (FTIR) spectra (Perkin-Elmer, Spectrum RX I). The amine group
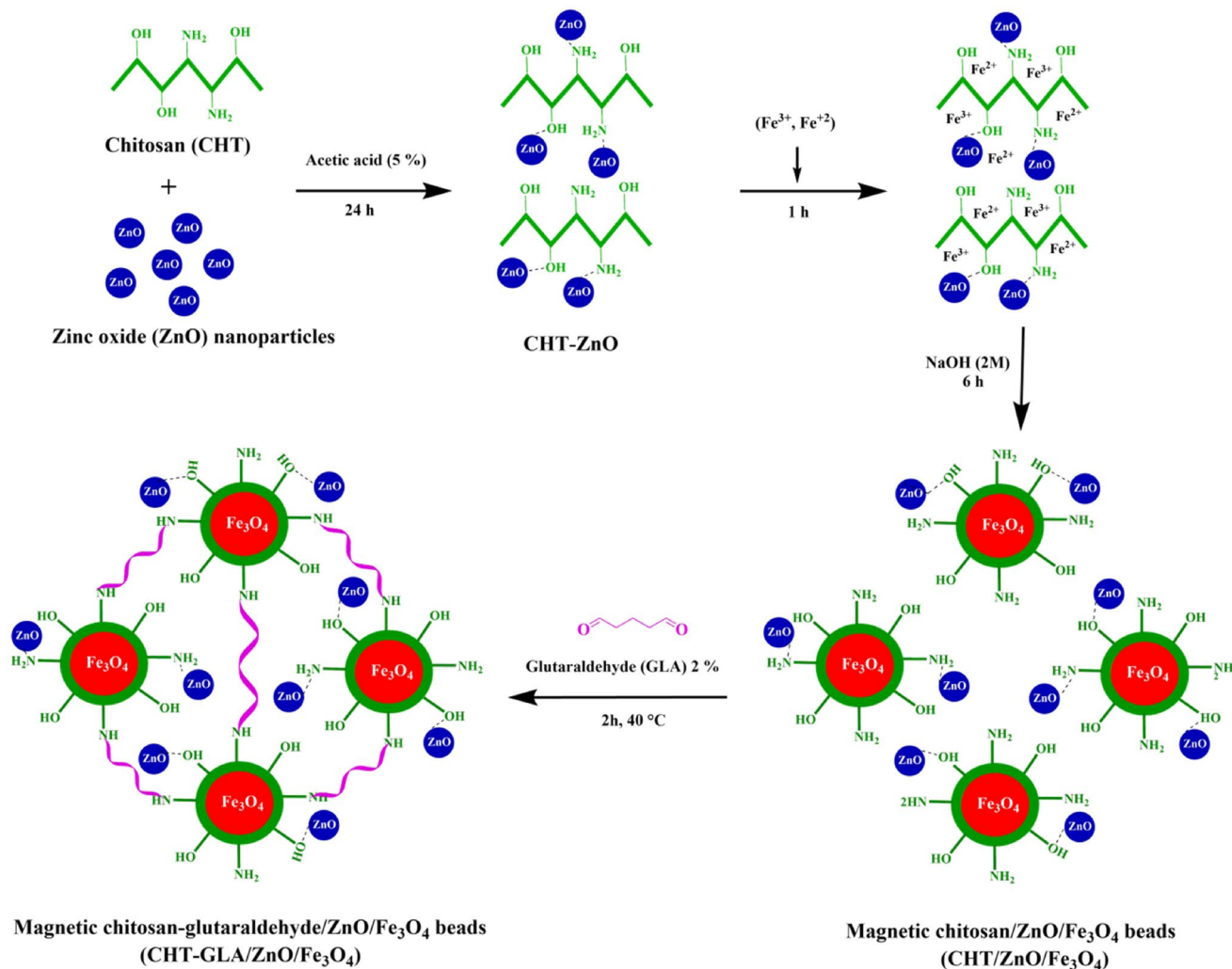

Fig. 1 Synthesis steps of CHT-GLA/ZnO/Fe_3O_4

content of the synthesized composites was identified by pH-potentiometric titration mode [32]. The surface charge of the CHT-GLA/ZnO/Fe$_3$O$_4$-25 was estimated by zero point of charge (pH$_{pzc}$) analysis [33]. The C, H, and N contents in the synthesized composites were determined by a CHN analyzer (Thermo Scientific).

Experimental Setup

In this study, BBD was used as an efficient and preferable statistical tool for generating the RBBR removal efficiency (%) as the response regarding response-dependent factors including ZnO loading, dose, pH, temperature, and time. Stat-Ease Design-Expert (Version 11) software was appointed to statistical analysis and mathematical modeling of the experimental data. Table 1 shows the experimental levels of independent variables and their codes. A polynomial equation (Eq. 1) was employed to fit the experimental data and predict the RBBR removal efficiency.

$$Y = \beta_0 + \sum \beta_i X_i + \sum \beta_{ii} X_i^2 + \sum \sum \beta_{ij} X_i X_j \qquad (1)$$

where Y, and (X_i and X_j) denote the predicted response, and coded values of factors. β_0, β_i, β_{ii} and β_{ij} indicate the regression coefficients of intercept, the linear, quadratic, and the interaction effects, respectively. Forty-six experiments were obtained through BBD model to investigate the impacts of the five variables: A: ZnO loading (0–50%), B: dose (0.02–0.1 g), C: pH (4–10), D: temperature (30–60 °C), and E: time (10–60 min) on the RBBR removal efficiency. Table 2 displays the experiments for the optimization as per BBD and their experimental responses. A known mass of adsorbent was added to 250 mL conical flasks, which contained a 100 mL of RRBR solution. The flasks were sealed and shaken by a shaker bath incubator (WNB7-45, Memmert) at shaking speed of 100 strokes/min. After adsorption, the adsorbent material was magnetically separated by external magnetic field, and the resulting solution was filtered with a 0.45 μm syringe filter. The RBBR concentrations in solution were calculated spectrophotometrically at λ_{max} 592 nm by UV–Vis spectroscopy. Equation (2) shows the relationship for calculating the RBBR removal efficiency (RE %).

$$RE\% = \frac{(C_o - C_e)}{C_o} \times 100 \qquad (2)$$

where C_o (mg/L) and C_e (mg/L) denote the RRBR concentrations at initial and at equilibrium, respectively.

Adsorption Study of RBBR by CHT-GLA/ZnO/Fe$_3$O$_4$

Batch experiments were performed to calculate the adsorption capacity of CHT-GLA/ZnO/Fe$_3$O$_4$-25. According to Table 2, the greatest removal of RBBR was recorded in experiment seven under these conditions: ZnO loading = 25%, dose = 0.06 g, pH 4, temperature = 60 °C, and time = 35 min. Thus, the experiments of the RBBR dye adsorption were conducted with these conditions stated above at different initial RBBR concentrations (50–250 mg/L) and contact time (0–540 min). Equation (3) gives the relationship for calculating the adsorption capacity, q_e (mg/g) of RBBR by CHT-GLA/ZnO/Fe$_3$O$_4$ at equilibrium.

$$q_e = \frac{(C_o - C_e)V}{W} \qquad (3)$$

where W and V denote the mass of the used composite (g) and the volume of the RRBR solution (L), respectively.

Results and Discussion

Characterization of the Prepared Magnetic Adsorbents

The physicochemical characteristics, namely, elemental composition, amine group content, surface areas properties of the CHT-GLA/Fe$_3$O$_4$, CHT-GLA/ZnO/Fe$_3$O$_4$-25, CHT-GLA/ZnO/Fe$_3$O$_4$-50 are presented in Table 3. CHN-O analysis of the elemental composition demonstrated that the CHT-GLA/ZnO/Fe$_3$O$_4$-25 and CHT-GLA/ZnO/Fe$_3$O$_4$-50 had lower carbon content, and higher oxygen content than CHT-GLA/Fe$_3$O$_4$. This finding can be attributed to the incorporation of metal oxide (ZnO) nanoparticles into the molecular structure of CHT-GLA. The results of the pH-potentiometric titration clarified that the amine group content (%) in CHT-GLA/ZnO/Fe$_3$O$_4$-25 and CHT-GLA/ZnO/Fe$_3$O$_4$-50 was gradually decreased with additional loading of ZnO nanoparticles in the molecular structure of CHT-GLA. This observation can be assigned to the physical mixing of CHT with ZnO nanoparticles. In another word, more loading of ZnO nanoparticles will lead to less content of CHT in the whole molecular structure of the composite material as a result less amine group content will be obtained [15]. Another possible reason is the coordination of zinc ions with

Table 1 Coded and actual variables and their levels in BBD

Codes	Variables	Level 1 (−1)	Level 2 (0)	Level 3 (+1)
A	ZnO loading (%)	0	25	50
B	Dose (g)	0.02	0.06	0.1
C	pH	4	7	10
D	Temperature (°C)	30	45	60
E	Time (min)	10	35	60

Table 2 The 5-varibles BBD matrix and experimental data for RBBR removal

Run	A:ZnO loading	B:Dose	C:pH	D:Temp	E:Time	RBBR removal (%)
1	0	0.02	7	45	35	10.2
2	50	0.02	7	45	35	42.6
3	0	0.1	7	45	35	41.6
4	50	0.1	7	45	35	50.3
5	25	0.06	4	30	35	65.1
6	25	0.06	10	30	35	29.1
7	25	0.06	4	60	35	75.8
8	25	0.06	10	60	35	39.4
9	25	0.02	7	45	10	32.2
10	25	0.1	7	45	10	44.9
11	25	0.02	7	45	60	22.7
12	25	0.1	7	45	60	62.9
13	0	0.06	4	45	35	42.3
14	50	0.06	4	45	35	57.2
15	0	0.06	10	45	35	18.9
16	50	0.06	10	45	35	43.2
17	25	0.06	7	30	10	40.3
18	25	0.06	7	60	10	41.8
19	25	0.06	7	30	60	52.2
20	25	0.06	7	60	60	52.9
21	25	0.02	4	45	35	35.2
22	25	0.1	4	45	35	74.1
23	25	0.02	10	45	35	27.6
24	25	0.1	10	45	35	38.7
25	0	0.06	7	30	35	39.2
26	50	0.06	7	30	35	45.1
27	0	0.06	7	60	35	35.2
28	50	0.06	7	60	35	45.9
29	25	0.06	4	45	10	69.1
30	25	0.06	10	45	10	27.7
31	25	0.06	4	45	60	64.4
32	25	0.06	10	45	60	43.3
33	0	0.06	7	45	10	36.3
34	50	0.06	7	45	10	41.7
35	0	0.06	7	45	60	30.6
36	50	0.06	7	45	60	50.3
37	25	0.02	7	30	35	27.1
38	25	0.1	7	30	35	59.5
39	25	0.02	7	60	35	30.9
40	25	0.1	7	60	35	63.6
41	25	0.06	7	45	35	42.2
42	25	0.06	7	45	35	43.2
43	25	0.06	7	45	35	45.2
44	25	0.06	7	45	35	48.2
45	25	0.06	7	45	35	46.2
46	25	0.06	7	45	35	50.2

Table 3 The physicochemical properties of the synthesized nanocomposites

Analysis	CHT-GLA/Fe$_3$O$_4$	CHT-GLA/ZnO/Fe$_3$O$_4$-25	CHT-GLA/ZnO/Fe$_3$O$_4$-50
C (wt%)	33.95	26.34	17.92
H (wt%)	6.37	4.97	3.15
N (wt%)	4.19	2.93	1.49
O (wt%) (by difference)	55.49	62.76	77.44
-NH$_2$ content (%)	26.5	19.3	16.1
BET surface area (m^2/g)	4.17	9.92	6.67
Total pore volume (cm^3/g)	0.0129	0.0180	0.0170
V$_m$ (cm^3/g)	0.00033	0.00069	0.00037
Mean pore diameter (nm)	12.3	7.2	10.2

the amino and hydroxyl groups, which may lead to reduce the free amino group content [29].

The results of BET analysis show that the surface area of CHT-GLA/Fe$_3$O$_4$, CHT-GLA/ZnO/Fe$_3$O$_4$-25, and CHT-GLA/ZnO/Fe$_3$O$_4$-50 are 4.17 m^2/g, 9.92 m^2/g, and 6.67 m^2/g, respectively. These results are probably because the ZnO nanoparticles possessing a high surface area were scattered on the CHT-GLA/Fe$_3$O$_4$ matrix and enlarged its surface [34]. It was clearly observed from Table 3 that the CHT-GLA/ZnO/Fe$_3$O$_4$-25 has a higher surface area compared to CHT-GLA/ZnO/Fe$_3$O$_4$-50, although CHT-GLA/ZnO/Fe$_3$O$_4$-50 has a higher loading of ZnO nanoparticles. These results can be attributed to the fact that a high loading of ZnO nanoparticles may cause depositing of some of them within the larger pores of the CHT-GLA matrix [35]. Depending on the classification of IUPAC, all the prepared composites (CHT-GLA/Fe$_3$O$_4$, CHT-GLA/ZnO/Fe$_3$O$_4$-25, and CHT-GLA/ZnO/Fe$_3$O$_4$-50) are a mesoporous [36].

The crystallinity of the CHT-GLA/Fe$_3$O$_4$, CHT-GLA/ZnO/Fe$_3$O$_4$-25, and CHT-GLA/ZnO/Fe$_3$O$_4$-50 were investigated by XRD analysis. The XRD patterns of CHT-GLA/Fe$_3$O$_4$, CHT-GLA/ZnO/Fe$_3$O$_4$-25, and CHT-GLA/ZnO/Fe$_3$O$_4$-50 are exhibited respectively in Fig. 2a–c. The XRD result of CHT-GLA/Fe$_3$O$_4$ (Fig. 2a) exhibits several crystalline peaks at 2θ = 30.1°, 35.2°, 43.1°, 53.2°, 57.3°, and 62.1°, which are assigned to (220), (311), (400), (422), (511), and (440) of Fe$_3$O$_4$ particles, respectively (JCPDS card No. 19-629) [37]. The broad peak observed at 20.3° in Fig. 2a is ascribed to the semicrystalline nature of CHT [38]. The XRD patterns of CHT-GLA/ZnO/Fe$_3$O$_4$-25 (Fig. 2b) and CHT-GLA/ZnO/Fe$_3$O$_4$-50 (Fig. 2c) shows a typical crystalline peak at 31.80, 34.45, 36.27, 47.59, 56.66, 62.91, and 68.0 belonging to the crystalline phases (100), (002), (101), (102), (110), (103), and (112), respectively of ZnO nanoparticles (JCPDS card no. 36-1451) [38]. These results confirm the strong interaction between the -NH$_2$ and -OH groups of CHT with Zn ions and reinforce a good compatibility between the polymer matrix of CHT-GLA and the
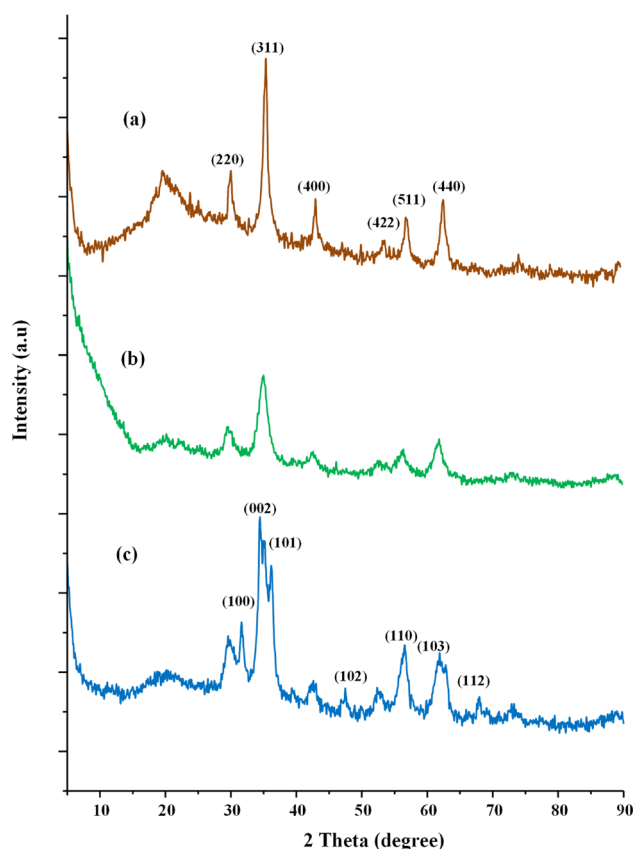

Fig. 2 XRD patterns of **a** CHT-GLA/Fe$_3$O$_4$, **b** CHT-GLA/ZnO/Fe$_3$O$_4$-25, and **c** CHT-GLA/ZnO/Fe$_3$O$_4$-50

ZnO [39]. Furthermore, it was noticed that all the peaks of CHT-GLA/ZnO/Fe$_3$O$_4$-50 had a higher intensity compared to CHT-GLA/ZnO/Fe$_3$O$_4$-25 due to the increased loading of ZnO nanoparticles in the polymer matrix of CHT-GLA.

The typical functional groups of the CHT-GLA/Fe$_3$O$_4$, CHT-GLA/ZnO/Fe$_3$O$_4$-25, and CHT-GLA/ZnO/Fe$_3$O$_4$-25 after RBBR adsorption were obtained by FTIR analysis. The FTIR spectra of CHT-GLA/Fe$_3$O$_4$, CHT-GLA/ZnO/
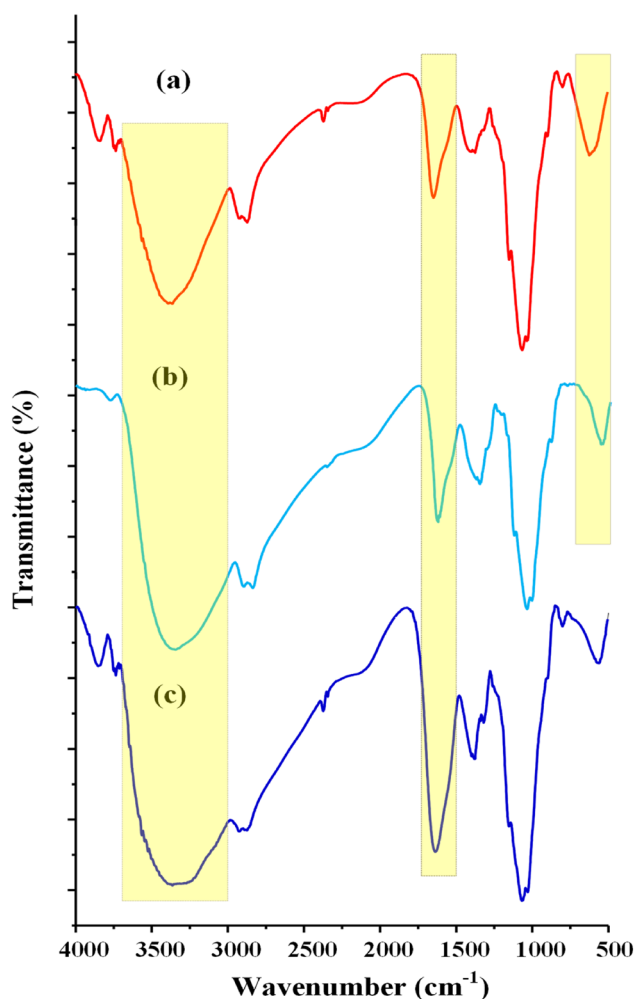
Fig. 3 FTIR spectra of **a** CHT-GLA/Fe$_3$O$_4$, **b** CHT-GLA/ZnO/Fe$_3$O$_4$-25, and **c** CHT-GLA/ZnO/Fe$_3$O$_4$-25 after adsorption of RBBR dye

Fe$_3$O$_4$-25, and CHT-GLA/ZnO/Fe$_3$O$_4$-25 after RBBR adsorption are presented respectively in Fig. 3a–c. The bands observed (Fig. 3a) at 3430 cm^{-1}, 2910 cm^{-1}, 1640 cm^{-1}, 1370 cm^{-1}, 1060 cm^{-1}, and 550 cm^{-1} are ascribed to O–H and N–H stretching, C–H symmetric stretching, N–H bending vibration, C–N stretching of residual N-acetyl group, C–O–C stretching vibration, and Fe–O bond, respectively [40]. The peak at 1660 cm^{-1} also corresponding to the C=N stretching vibration arising from Schiff base reaction between amino groups of CHT and carbonyl groups of GLA [15]. In FTIR spectrum of CHT-GLA/ZnO/Fe$_3$O$_4$-25, it was clearly observed the bands of –NH$_2$ and –OH groups were shifted and became stronger, signifying the strong interaction between –NH$_2$ and –OH groups and ZnO [38]. In same context, the peak observed at 540 cm^{-1} corresponding to metaloxygen linkage (Zn–O) [41]. The spectrum of the

CHT-GLA/ZnO/Fe$_3$O$_4$ nanocomposite after RRBR adsorption appeared a remarkable shift in the –OH and N–H bands, signifying the contributing of the –OH and NH$_2$ groups in the RBBR adsorption.

The surface morphology and chemical composition of CHT-GLA/Fe$_3$O$_4$, CHT-GLA/ZnO/Fe$_3$O$_4$-25, CHT-GLA/ZnO/Fe$_3$O$_4$-50, and CHT-GLA/ZnO/Fe$_3$O$_4$-25 after RBBR adsorption were examined by SEM–EDX. The SEM images and EDX analysis of CHT-GLA/Fe$_3$O$_4$, CHT-GLA/ZnO/Fe$_3$O$_4$-25, CHT-GLA/ZnO/Fe$_3$O$_4$-50, and CHT-GLA/ZnO/Fe$_3$O$_4$-25 after RBBR adsorption are presented respectively in Fig. 4a–d. As depicted in Fig. 4a, the CHT-GLA/Fe$_3$O$_4$ nanocomposite owned an irregular, wavy, and uneven structure. The EDX analysis of CHT-GLA/Fe$_3$O$_4$ composite detects the presence of C, O, N and Fe. Figure 4b and Fig. 4c corresponding to 25% ZnO and 50% ZnO nanoparticles loaded into molecular structure of CHT-GLA show that the nanocomposite's surface contains small fractures and holes due to the embedded and well-dispersed ZnO nanoparticles into polymer matrix of CHT-GLA. According to EDX analysis, the main elements present in CHT-GLA/ZnO/Fe$_3$O$_4$-25 and CHT-GLA/ZnO/Fe$_3$O$_4$-50 nanocomposites are C, N, O, Fe and Zn. The presence of peak for Zn element in the EDX spectrum confirms that the ZnO nanoparticles were successfully loaded into the structure of CHT-GLA. After RRBR adsorption (Fig. 4d), CHT-GLA/ZnO/Fe$_3$O$_4$ nanocomposite surface was remarkably changed into smooth, compact, and homogenous surface in agreement with the covering by RBBR molecule. This finding was confirmed by EDX, which indicated the existence S element.

Statistical Analysis and Model Fitting

The statistical analysis and specification the important impacts of the parameters and their interactions for the RBBR removal data was achieved by the variance analysis (ANOVA). Table 4 displays ANOVA results of the RBBR removal. The model F value of 16.37 (p-value < 0.0001) indicates that the model for the RBBR removal is significant [42]. The value of correlation coefficient (R^2) for this model is 0.93, which indicates that the accuracy of the fitting of the model, and good correlation between predicted and experimental RBBR removal values [22]. Statistically, the model terms are significant with P-value less than 0.05. In this case A, B, C, E, AB, BC, BE, A^2, and B^2 are significant terms in the RBBR removal process. Thus, the experimental relationship between RBBR removal efficiency and the examined variables was correlated by quadratic polynomial model as expressed in Eq. (4).
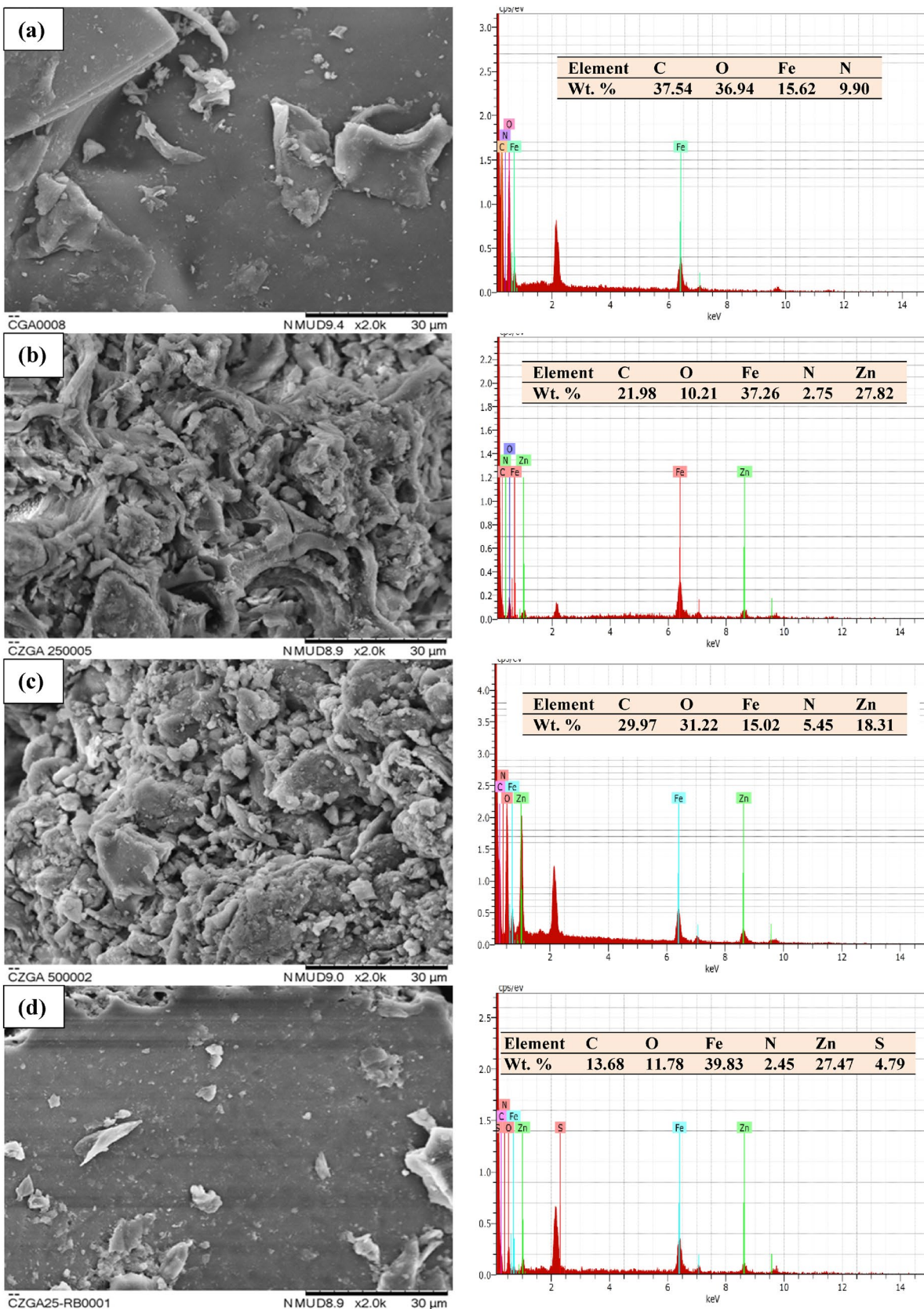
Fig. 4 SEM images of **a** CHT-GLA/Fe$_3$O$_4$, **b** CHT-GLA/ZnO/Fe$_3$O$_4$-25, **c** CHT-GLA/ZnO/Fe$_3$O$_4$-50, and **d** CHT-GLA/ZnO/Fe$_3$O$_4$-25 after adsorption of RBBR dye at magnification power 2000x

Table 4 Analysis of variance (ANOVA) for RBBR removal

Source	Sum of Squares	df	Mean Square	F-value	p-value
Model	8308.45	20	415.42	16.37	< 0.0001
A-ZnO loading	930.25	1	930.25	36.65	< 0.0001
B-Dose	2680.65	1	2680.65	105.63	< 0.0001
C-pH	2897.13	1	2897.13	114.16	< 0.0001
D-Temperature	48.65	1	48.65	1.92	0.1784
E-Time	128.26	1	128.26	5.05	0.0336
AB	140.42	1	140.42	5.53	0.0268
AC	22.09	1	22.09	0.8704	0.3598
AD	5.76	1	5.76	0.2270	0.6379
AE	51.12	1	51.12	2.01	0.1682
BC	193.21	1	193.21	7.61	0.0107
BD	0.0225	1	0.0225	0.0009	0.9765
BE	189.06	1	189.06	7.45	0.0115
CD	0.0400	1	0.0400	0.0016	0.9686
CE	103.02	1	103.02	4.06	0.0548
DE	0.1600	1	0.1600	0.0063	0.9373
A^2	411.25	1	411.25	16.20	0.0005
B^2	144.77	1	144.77	5.70	0.0248
C^2	88.09	1	88.09	3.47	0.0742
D^2	55.00	1	55.00	2.17	0.1535
E^2	0.0064	1	0.0064	0.0003	0.9875
Residual	634.47	25	25.38		
Cor Total	8942.91	45			

RBBR removal efficiency (%)

$$= +45.87 + 7.63A + 12.94B - 13.46C + 2.83E$$
$$- 5.93AB - 6.95BC + 6.88BE - 6.86A^2 - 4.07B^2 \quad (4)$$

Moreover, the verification of experimental results can be achieved by the analysis of the obtained graphics from BBD model such as actual versus predicted, normal probability of the residuals, and externally studentized residuals versus predicted. Figure 5a displays the actual versus predicted plot of RBBR removal efficiency values. According to Fig. 5a, the points of actual were mostly close to the points of predicted, signifying that the BBD model can adequately optimize the adsorption process of RBBR dye. Figure 5b demonstrates the normal probability plot of residuals. As per Fig. 5b, all points are normally distributed around the straight-line, elucidating that the independence of the residuals [37]. Figure 5c shows the plot of externally studentized residuals of the experimental versus predicted values. It can be noticed from Fig. 5c the points are scattered around the horizontal line, indicating that no significant variation between actual and predicted [43].

Optimization of RBBR Removal

Three-dimensional (3D) response surfaces are important graphical plots to explain the interaction effects of two operational factors on the RBBR removal efficiency. Figure 6a presents the 3D surface plot of the combined effect of ZnO loading and dose on the RBBR removal efficiency at a constant pH (7), temperature (45 °C), and time (35 min). The obtained results from Fig. 6a demonstrate that the RBBR removal efficiency was improved by increasing both adsorbent dose and ZnO loading. This finding relates to the high surface area resulted from ZnO nanoparticles and the higher number of active binding sites of the CHT-GLA/ZnO/Fe$_3$O$_4$, which are readily available to adsorb RBBR dye [35].

Figure 6b presents the 3D surface plot of the combined effect of dose and pH on the RBBR removal efficiency at a constant ZnO loading (25%), temperature (45 °C), and time (35 min). It can be seen from Fig. 6b, the RBBR removal efficiency (%) increased by decreasing the pH value from basic environment (pH 10) towards acidic environment (pH 4). The value pH$_{pzc}$ of the CHT-GLA/ZnO/Fe$_3$O$_4$ is 7.4 as illustrated in Fig. 6c. This finding signifies that the CHT-GLA/ZnO/Fe$_3$O$_4$ surface at pH value greater than pH$_{pzc}$ acquires a negative charge. Thus, the CHT-GLA/ZnO/Fe$_3$O$_4$ surface at acidic environment (pH 4) turns to a positive charge due to the increase of H$^+$ concentration in the solution [44]. Accordingly, electrostatic attractions will be formed between the surface cationic groups of the CHT-GLA/ZnO/Fe$_3$O$_4$ and the RBBR molecules as outlined in Eq. (5).

$$CHT - GLA/ZnO/Fe_3O_4^+ + RBBR^- \; CHT - GLA/ZnO/Fe_3O_4^+ \ldots {}^-RBBR \quad (5)$$
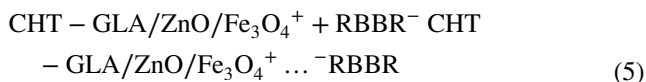
The combined effect of dose and time on the RBBR removal efficiency was important. Figure 6d presents the 3D surface plot of the important combined effects of dose and time on the RBBR removal efficiency at a constant ZnO loading (25%), pH (7), and temperature (45 °C). As can be shown from Fig. 6d that the RBBR removal efficiency did not improve significantly by increasing the contact time up to 60 min, indicating that the occupancy of the active sites on the adsorbent with RBBR molecules was extremely fast, and reached the equilibrium absorption of RBBR dye within a short period of time.

Adsorption Study

The time dependence of RBBR uptake by CHT-GLA/ZnO/Fe$_3$O$_4$-25 nanocomposite was monitored for better understanding to the adsorption process. In this regard, the influence of different initial RBBR concentration (range
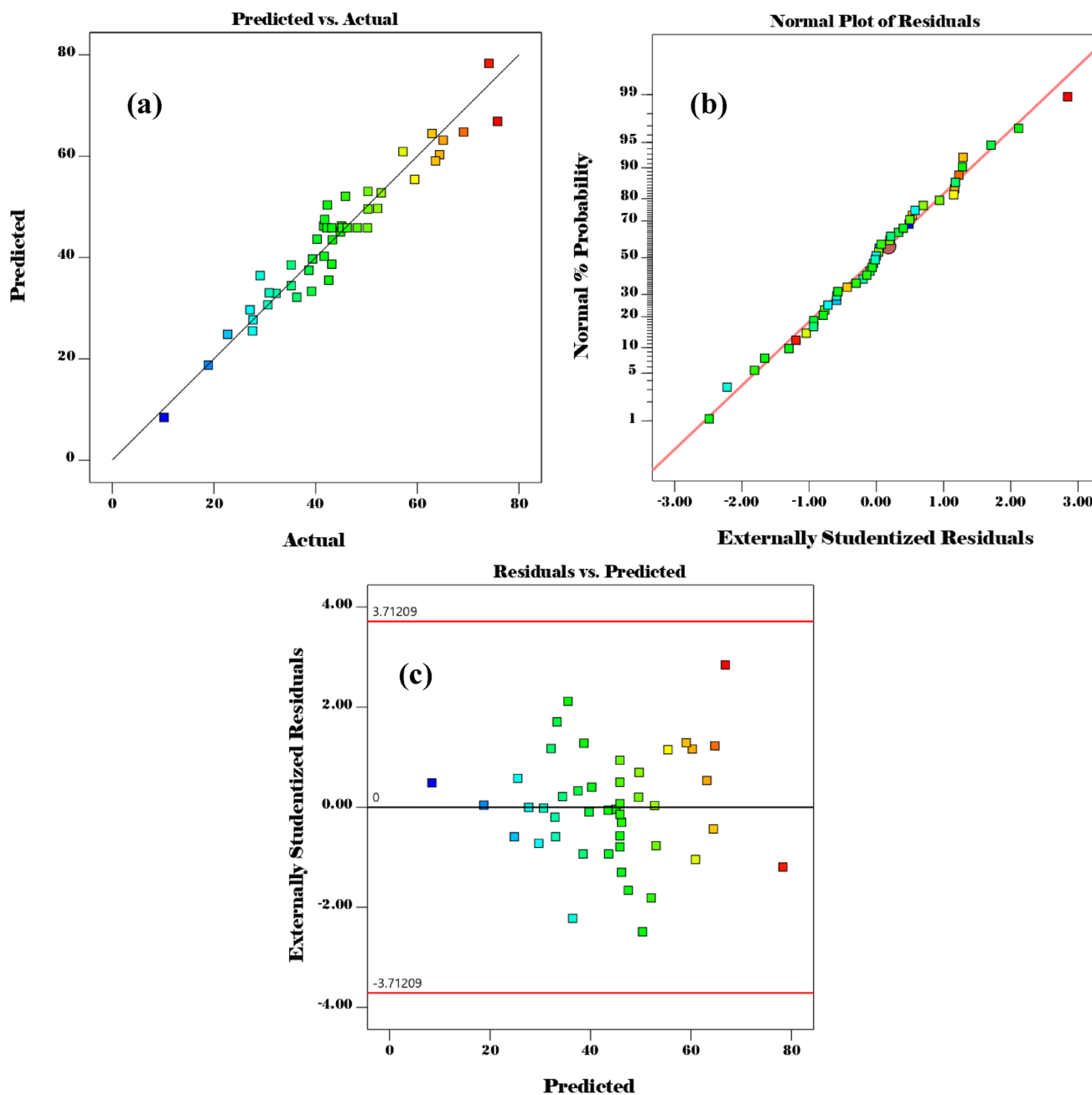
Fig. 5 Plots of **a** actual versus predicted, **b** normal probability of the residuals, and **c** externally studentized residuals versus predicted

50–250 mg/L) on adsorption behaviour of RBBR by CHT-GLA/ZnO/Fe$_3$O$_4$-25 nanocomposite was investigated at fixed dose of CHT-GLA/ZnO/Fe$_3$O$_4$-25 (0.06 g), temperature (60 °C), solution pH (4), and solution volume (100 mL). The adsorption capacity values of CHT-GLA/ZnO/Fe$_3$O$_4$-25 as a function of contact time were presented in Fig. 7a. As can be seen, rapid q_t increases at the beginning of the adsorption process for all studied concentrations which can be attributed to the existence of the adsorption active groups on the surface of CHT-GLA/ZnO/Fe$_3$O$_4$-25, indicating

CHT-GLA/ZnO/Fe$_3$O$_4$-25 could be utilized as a promising adsorbent in textile dye removal. Moreover, the adsorption capacity of CHT-GLA/ZnO/Fe$_3$O$_4$-25 was found to increase from 60.6 to 176.6 mg/g by increasing the initial RBBR concentration from 50 to 250 mg/L. This result may be due to the higher RBBR concentration gradient, which enhances the moving of RBBR molecules to the active sites available onto the CHT-GLA/ZnO/Fe$_3$O$_4$-25 surface [13, 45].
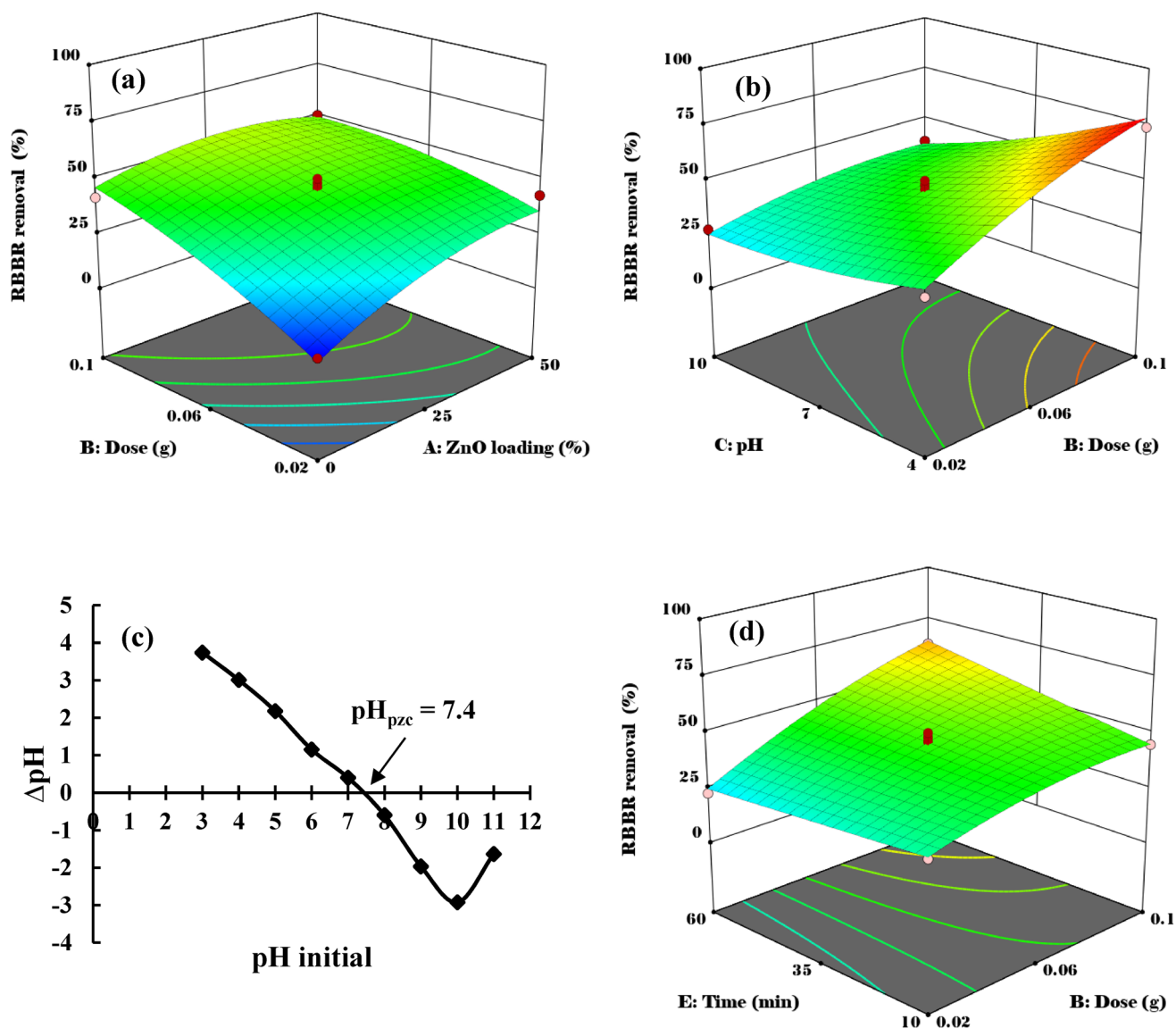
Fig. 6 3D plots of **a** AB, **b** BC, and **d** BE significant interactions on RBBR removal; whereas. **c** pH$_{pzc}$ of CHT-GLA/ZnO/Fe$_3$O$_4$

Kinetic Study

To determine the controlling mechanism of the adsorption process of the RBBR on the CHT-GLA/ZnO/Fe$_3$O$_4$ surface. The dynamical experimental data were fitted to two kinetic models: pseudo-first order (PFO) [46] and pseudo-second order (PSO) [47]. The parameters of the kinetic models were obtained by the non-linear equations of PFO and PSO given in Eqs. (6) and (7) respectively.

$$q_t = q_e(1 - \exp^{-k_1 t}) \tag{6}$$

$$q_t = \frac{q_e^2 k_2 t}{1 + q_e k_2 t} \tag{7}$$

where q_e and q_t are the adsorption capacities (mg/g) at adsorption equilibrium and time (t), respectively. k_1 (1/min) is the PFO adsorption rate constant and k_2 (g/mg min) is the PSO adsorption rate constant. The calculated parameters of the kinetic models are listed in Table 5. It can be seen from Table 5 that the R^2 values of the PSO was higher than the PFO. Moreover, the calculated q_e of the PSO was closer to the experimental q_e compared to the values of calculated q_e for the PFO. The obtained results clarified that the adsorption of RBBR dye onto CHT-GLA/ZnO/Fe$_3$O$_4$ surface is a chemisorption process including electrostatic interactions, which are happened between the positive charges and cationic groups available on the CHT-GLA/ZnO/Fe$_3$O$_4$ nanocomposite surface with the negative charges (–SO$_3^-$) of the RBBR dye [48].
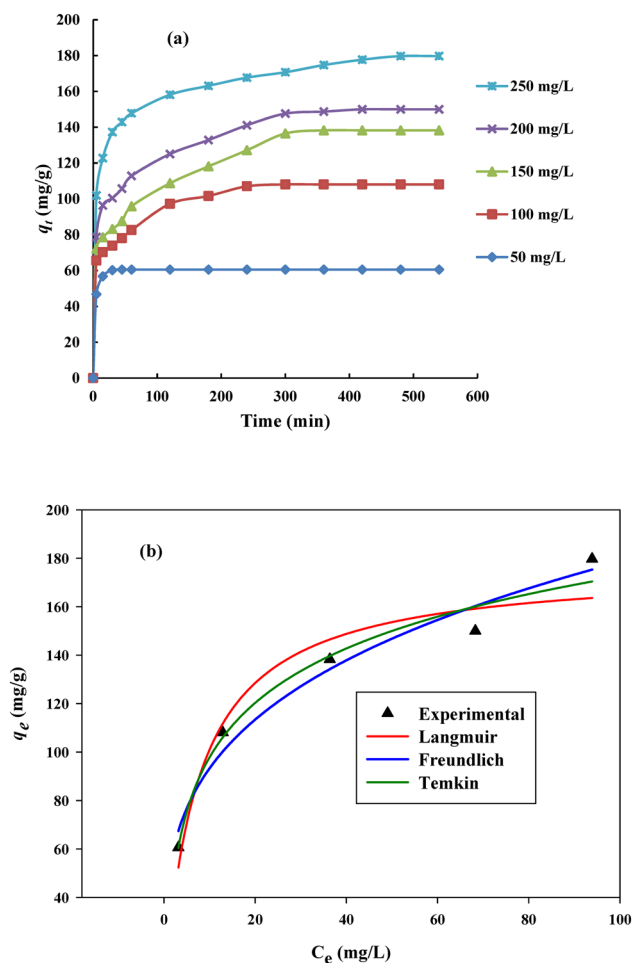
Fig. 7 **a** Effect of the contact time on RBBR dye adsorption at different initial concentrations and **b** adsorption isotherms of RBBR by CHT-GLA/ZnO/Fe$_3$O$_4$-25 (dosage 0.06 g, pH of solution 4, temperature 60 °C, agitation speed = 100 stroke/min and volume of solution = 100 mL)

Isotherm Study

The adsorption isotherms are applied to understand the relationship between equilibrium adsorption capacity of the CHT-GLA/ZnO/Fe$_3$O$_4$ nanocomposite and initial concentration of RBBR [13]. The equilibrium adsorption is crucial parameter in the describing and explaining the correlation between CHT-GLA/ZnO/Fe$_3$O$_4$ nanocomposite and RBBR molecules. The affinity and adsorption capacity of CHT-GLA/ZnO/Fe$_3$O$_4$-25 nanocomposite to adsorb RBBR dye from aqueous solution were elucidated by fitting the experimental data to Langmuir [49], Freundlich [50], and Temkin [51] isotherm models. The Langmuir model indicates that all adsorption sites are equivalent and a monolayer adsorption towards pollutants is occurred on a homogeneous surface of adsorbent [13]. The Freundlich model is generally used to describe a multilayer adsorption

Table 5 PFO and PSO kinetic parameters for RBBR dye adsorption on CHT-GLA/ZnO/Fe$_3$O$_4$-25

Concentration (mg/L)	$q_{e\,exp}$ (mg/g)	PFO			PSO		
		$q_{e\,cal}$ (mg/g)	k_1 (1/min)	R^2	$q_{e\,cal}$ (mg/g)	$k_2 \times 10^{-2}$ (g/mg min)	R^2
50	60.6	60.3	0.292	0.99	61.3	1.152	0.99
100	108.1	97.9	0.139	0.80	104.6	0.154	0.91
150	138.3	126.8	0.044	0.77	133.1	0.063	0.98
200	150.0	135.1	0.091	0.82	143.8	0.089	0.93
250	179.7	163.2	0.139	0.90	176.5	0.116	0.97

towards pollutants is occurred on a heterogeneous surface of adsorbent [18, 19]. Moreover, the Temkin model assumes there is a linear relationship between adsorption heat and coverage by taking into consideration the temperature effect [17]. The parameters of the isotherms were obtained by the non-linear equations of Langmuir, Freundlich, and Temkin as presented in Eqs. (8), (9), and (10) respectively.

$$q_e = \frac{q_{max} K_a C_e}{1 + K_a C_e} \qquad (8)$$

$$q_e = K_f C_e^{1/n} \qquad (9)$$

$$q_e = \frac{RT}{b_T} \ln(K_T C_e) \qquad (10)$$

where q_{max} (mg/g) is the calculated adsorption capacity of the CHT-GLA/ZnO/Fe$_3$O$_4$, and K_a (L/mg) is the Langmuir equilibrium constant. K_f (mg/g) (L/mg)$^{1/n}$ and n are constants related to the Freundlich model. K_T (L/mg) and b_T (J/mol) are Temken constants related to the equilibrium

binding, and adsorption heat. T (K) and R (8.314 J/mol K) represents the temperature and gas constant, respectively. Figure 7b and Table 6 show the fitting parameters and curves of isotherms, respectively. As per the correlation coefficient (R^2) of models, the Freundlich model ($R^2 = 0.97$) and Temkin model ($R^2 = 0.97$) are higher than that of the Langmuir model ($R^2 = 0.94$), Thus, the adsorption process of RBBR by CHT-GLA/ZnO/Fe$_3$O$_4$ is more in line with the Freundlich and Temkin models, indicating the heterogeneous character of the RBBR physical and chemical adsorption onto CHT-GLA/ZnO/Fe$_3$O$_4$ surface [52]. The q_{max} of RBBR on CHT-GLA/ZnO/Fe$_3$O$_4$-25 was found as 176.6 mg/g at 60 °C. Table 7 summarizes the comparison the q_{max} of the CHT-GLA/ZnO/Fe$_3$O$_4$-25 with other adsorbents reported in previous works toward RBBR. These results of Table7 demonstrate that the CHT-GLA/ZnO/Fe$_3$O$_4$-25 had favorable adsorption ability for the removal of organic dyes from wastewater.

Adsorption Mechanism of RBBR

The adsorption mechanism of RBBR on the CHT-GLA/ZnO/Fe$_3$O$_4$ nanocomposite surface was sketched depending on of the presence of active adsorption sites such as hydroxyl (–OH), amino (–NH$_2$) and Zn (OH)$^+$, as shown in Fig. 8. At first, CHT-GLA/ZnO/Fe$_3$O$_4$ nanocomposite surface can obtain positive charges in an acidic solution due to pH$_{acidic}$ < pH$_{pzc}$. The positive charges of the CHT-GLA/ZnO/Fe$_3$O$_4$ nanocomposite surface can be obtained from different sources such as hydroxyl (–OH), and amine (–NH$_2$) protonated groups, as well as positive charges formed from ZnO nanoparticles. Electrostatic interactions are prime character for the RBBR adsorption because of the plenty of positive charges and cationic groups on the CHT-GLA/ZnO/Fe$_3$O$_4$ nanocomposite surface, which are attracted with the negative charges (–SO$_3^-$) of the RBBR dye. Various studies have been reported using positive charges of ZnO nanoparticles formed in the acidic medium to adsorb organic dyes through electrostatic interactions [61, 62]. Hydrogen interactions

Table 6 Parameters of the Langmuir, Freundlich and Temkin isotherm models for RBBR dye adsorption on CHT-GLA/ZnO/Fe$_3$O$_4$-25 at 60 °C

Adsorption isotherm	Parameter	Value
Langmuir	q_{max} (mg/g)	176.6
	K_a (L/mg)	0.133
	R^2	0.94
Freundlich	K_f (mg/g) (L/mg)$^{1/n}$	48.76
	n	3.54
	R^2	0.97
Temkin	K_T (L/mg)	0.71
	b_T (J/mol)	85.4
	R^2	0.97

Table 7 Comparison of the adsorption capacity of RBBR dye by various adsorbents

Adsorbents	q_{max} (mg/g)	References
Magnetic chitosan-glutaraldehyde/zinc oxide/Fe$_3$O$_4$ nanocomposite	179.7	This study
Chitosan-tripolyphosphate/kaolin composite	687.2	[4]
Graphene oxide-ionic liquid	416.7	[53]
Sawdust-based activated carbon	368.5	[54]
Polyaniline/chitosan composite	303.03	[55]
ZnO-polyacrylonitrile-hinokitiol	267.37	[56]
Chitosan-alkali lignin composite	111.11	[57]
Chitosan/SiO$_2$/carbon nanotubes magnetic nanocomposite	97.08	[58]
Magnesium hydroxide coated bentonite	66.90	[59]
Borax cross-linked Jhingan gum hydrogel	9.884	[60]

Fig. 8 Illustration of the possible interaction between CHT-GLA/ZnO/Fe₃O₄ nanocomposite surface and RBBR dye including electrostatic attraction, hydrogen bonding interactions, Yoshida H-bonding, and n-π interactions
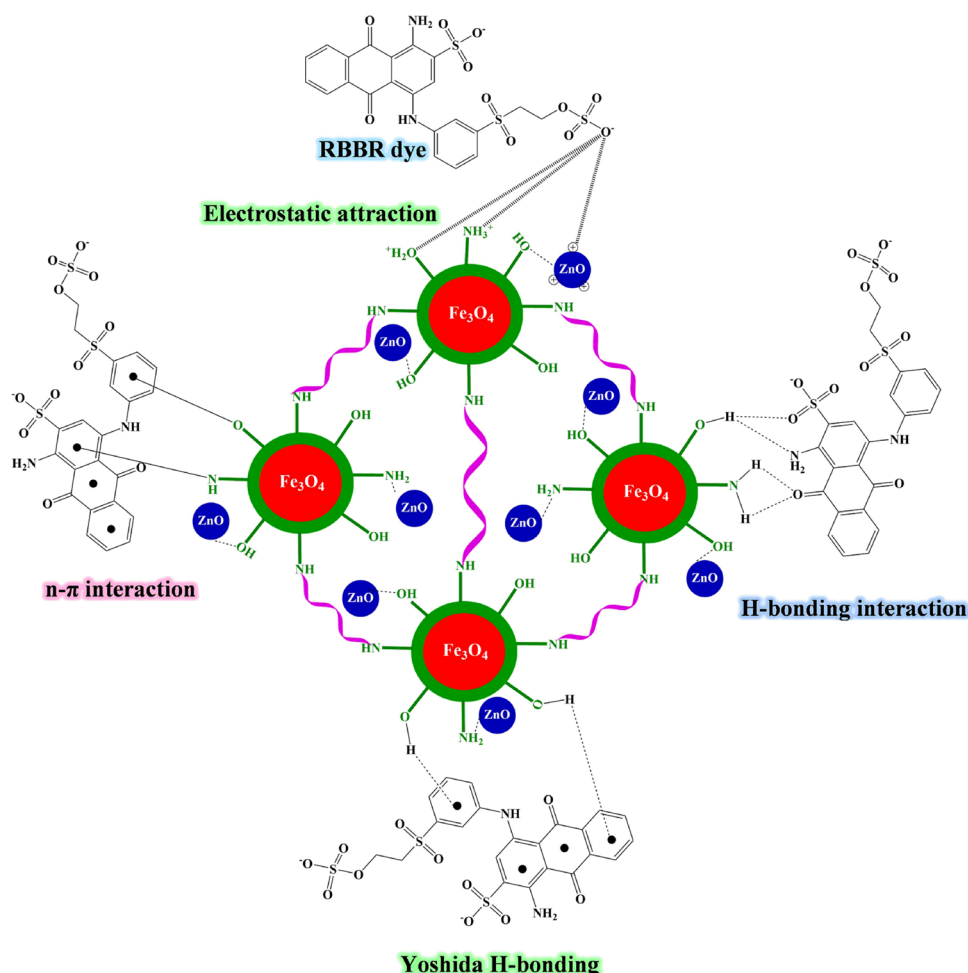
designated by H-bonding and Yoshida H-bonding from significant interactions that could be played an important role in adsorption of RBBR dye. These interactions (H-bonding) and (Yoshida H-bonding) are formed between the free H and H–OH (hydrogen of hydroxyl) available on the CHT-GLA/ZnO/Fe₃O₄ nanocomposite surface with N and O groups and the aromatic system of the RBBR dye, respectively [63]. Lastly, n–π interactions occur between the electron-donating system represented by groups containing N and O in the CHT-GLA/ZnO/Fe₃O₄ nanocomposite and the electron-accepting system represented by the aromatic rings of the RBBR dye [40].

Conclusion

A Schiff's base magnetic chitosan-glutaraldehyde/zinc oxide/Fe₃O₄ nanocomposite (CHT-GLA/ZnO/Fe₃O₄) was successfully developed to be an effective adsorbent for the removal of RBBR from RBBR dye solutions. The optimum conditions for synthesis of adsorbent and RBBR adsorption were ZnO nanoparticles loading (25%), dose (0.06 g), pH

(4), temperature (60 °C), and time (35 min). The obtained results from BBD demonstrated that the highest RBBR removal efficiency (75.8%) was recorded at AB (ZnO loading x adsorbent dosage), BC (adsorbent dosage x pH), and BE (adsorbent dosage x time) interactions. The experimental data of kinetics, isotherms showed that chemisorption and multilayer adsorption of the RBBR on the CHT-GLA/ZnO/Fe₃O₄-25 surface. The maximum adsorption capacity of the target nanocomposite (CHT-GLA/ZnO/Fe₃O₄-25) was reached of 176.6 mg/g at 60 °C. The adsorption mechanism of RBBR onto CHT-GLA/ZnO/Fe₃O₄ nanocomposite was attributed to multi-interactions including electrostatic attractions, hydrogen bonding, Yoshida H-bonding, and n-π interactions. This study presents a promising hybrid nanobiomaterial adsorbent in environmental nanotechnology to separate and remove the contaminants such as organic dyes from wastewater.

References

1. Pérez-Calderón J, Santos MV, Zaritzky N (2020) Synthesis, characterization and application of cross-linked chitosan/oxalic acid hydrogels to improve azo dye (Reactive Red 195) adsorption. React Funct Polym 155:104699

2. Rafaie HA, Yusop NFM, Azmi NF, Abdullah NS, Ramli NIT (2021) Photocatalytic degradation of methylene blue dye solution using different amount of ZnO as a photocatalyst. Sci Lett 15(1):1–12

3. Kueasook R, Rattanachueskul N, Chanlek N, Dechtrirat D, Watcharin W, Amornpitoksuk P, Chuenchom L (2020) Green and facile synthesis of hierarchically porous carbon monoliths via surface self-assembly on sugarcane bagasse scaffold: influence of mesoporosity on efficiency of dye adsorption. Micropor Mesopor Mater 296:110005

4. Jawad AH, Abdulhameed AS (2020) Facile synthesis of crosslinked chitosan-tripolyphosphate/kaolin clay composite for decolourization and COD reduction of remazol brilliant blue R dye: optimization by using response surface methodology. Colloids Surf A Physicochem Eng Asp 605:125329

5. Sathishkumar P, Arulkumar M, Palvannan T (2012) Utilization of agro-industrial waste Jatropha curcas pods as an activated carbon for the adsorption of reactive dye Remazol Brilliant Blue R (RBBR). J Clean Prod 22(1):67–75

6. Tang Q, Yang T, Wang S, Cong H-L, Yang X-R, Shen Y-Q, Yu B (2020) Facile light-assisted preparation of reusable magnetic Fe_3O_4@SiO_2@Chitosan composite for adsorption of dyes. Ferroelectrics 562:28–38

7. Wang Z, Si Z, Cai D, Li GLS, Qin P (2020) Synthesis of stable COF-300 nanofiltration membrane via in-situ growth with ultrahigh flux for selective dye separation. J Membr Sci 615:118466

8. Lakshmanan P, Thirumaran S, Ciattini S (2020) Synthesis, spectral and structural studies on NiS2PN and NiS2P2 chromophores and use of Ni (II) dithiocarbamate to synthesize nickel sulfide and nickel oxide for photodegradation of dyes. J Mol Struct 1220:128704

9. Mcyotto F, Wei Q, Macharia DK, Huang M, Shen C, Chow CW (2021) Effect of dye structure on color removal efficiency by coagulation. Chem Eng J 405:126674

10. Mashkoor F, Nasar A (2020) Magsorbents: Potential candidates in wastewater treatment technology: a review on the removal of methylene blue dye. J Magn Magn Mater 500:166408

11. Coura JC, Profeti D, Profeti LPR (2020) Eco-friendly chitosan/quartzite composite as adsorbent for dye removal. Mater Chem Phys 256:123711

12. Elshaarawy RF, Abd El-Azim H, Hegazy WH, Mustafa FH, Talkhan TA (2020) Poly (ammonium/pyridinium)-chitosan Schiff base as a smart biosorbent for scavenging of Cu^{2+} ions from aqueous effluents. Polym Test 83:106244

13. Zheng X, Zheng H, Xiong Z, Zhao R, Liu Y, Zhao C, Zheng C (2020) Novel anionic polyacrylamide-modify-chitosan magnetic composite nanoparticles with excellent adsorption capacity for cationic dyes and pH independent adsorption capability for metal ions. Chem Eng J 392:123706

14. Cai W, Zhu F, Liang H, Jiang Y, Tu W, Cai Z, Wu J, Zhou J (2019) Preparation of thiourea-modified magnetic chitosan composite with efficient removal efficiency for Cr (VI). J Chem Eng Data 144:150–158

15. Jiang Y, Cai W, Tu W, Zhu M (2019) A facile crosslink method to synthesize magnetic Fe_3O_4@SiO_2-chitosan with high adsorption capacity toward hexavalent chromium. J Chem Eng Data 64(1):226–233

16. Li Z, Li L, Hu D, Gao C, Xiong J, Jiang H, Li W (2019) Efficient removal of heavy metal ions and organic dyes with cucurbit [8] uril-functionalized chitosan. J Colloid Interface Sci 539:400–413

17. Chen Y, Cai W, Dang C, Fan J, Zhou J, Liu Z (2020) A facile sol–gel synthesis of chitosan–boehmite film with excellent acid resistance and adsorption performance for Pb(II). Chem Eng Res Des 161:332–339

18. Tanhaei B, Ayati A, Iakovleva E, Sillanpää M (2020) Efficient carbon interlayed magnetic chitosan adsorbent for anionic dye removal: Synthesis, characterization and adsorption study. Int J Biol Macromol 164:3621–3631

19. Guo M, Wang J, Wang C, Strong PJ, Jiang P, Ok YS, Wang H (2019) Carbon nanotube-grafted chitosan and its adsorption capacity for phenol in aqueous solution. Sci Tot Environ 682:340–347

20. Malek NNA, Yousif E, Jawad AH (2020) Optimization of adsorption parameters for reactive red 4 (RR4) removal by cross-linked chitosan-epichlorohydrin using Box Behnken Design. Sci Lett 14(1):83–95

21. Vithalkar SH, Jugade RM (2020) Adsorptive removal of crystal violet from aqueous solution by cross-linked chitosan coated bentonite. Mater Today Proceed 29:1025–1032

22. Abdulhameed AS, Mohammad AT, Jawad AH (2019) Application of response surface methodology for enhanced synthesis of chitosan tripolyphosphate/TiO2 nanocomposite and adsorption of reactive orange 16 dye. J Clean Prod 232:43–56

23. Sathiyavimal S, Vasantharaj S, Kaliannan T, Pugazhendhi A (2020) Eco-biocompatibility of chitosan coated biosynthesized copper oxide nanocomposite for enhanced industrial (Azo) dye removal from aqueous solution and antibacterial properties. Carbohydr Polym 241:116243

24. Ahmad H, Reduan SA, Yusoff N (2018) Nickel oxide nanoparticles grafted with Chitosan as saturable absorber for tunable passively Q-switched fiber laser in S+/S band. Infrared Phys Technol 93:96–102

25. Dil EA, Asfaram A, Goudarzi A, Zabihi E, Javadian H (2020) Biocompatible chitosan-zinc oxide nanocomposite based dispersive micro-solid phase extraction coupled with HPLC-UV for the determination of rosmarinic acid in the extracts of medical plants and water sample. Int J Biol Macromol 154:528–537

26. Amjadi S, Nazari M, Alizadeh SA, Hamishehkar H (2020) Multifunctional betanin nanoliposomes-incorporated gelatin/chitosan nanofiber/ZnO nanoparticles nanocomposite film for fresh beef preservation. Meat Sci 167:108161

27. Indumathi MP, Rajarajeswari GR (2019) Mahua oil-based polyurethane/chitosan/nano ZnO composite films for biodegradable food packaging applications. Int J Biol Macromol 124:163–174

28. Hassan H, Salama A, El-ziaty AK, El-Sakhawy M (2019) New chitosan/silica/zinc oxide nanocomposite as adsorbent for dye removal. Int J Biol Macromol 131:520–526

29. Ghaffari SB, Sarrafzadeh MH, Salami M, Khorramizadeh MR (2020) A pH-sensitive delivery system based on N-succinyl chitosan-ZnO nanoparticles for improving antibacterial and anticancer activities of curcumin. Int J Biol Macromol 151:428–440

30. Hassanein A, Salahuddin N, Matsuda A, Kawamura G, Elfiky M (2017) Fabrication of biosensor based on Chitosan-ZnO/Polypyrrole nanocomposite modified carbon paste electrode for electroanalytical application. Mater Sci Eng C 80:494–501

31. Maksoud MA, Elgarahy AM, Farrell C, Ala'a H, Rooney DW, Osman AI (2020) Insight on water remediation application using magnetic nanomaterials and biosorbents. Coord Chem Rev 403:213096

32. Vieira RS, Beppu MM (2006) Interaction of natural and crosslinked chitosan membranes with Hg (II) ions. Colloids Surf A Physicochem Eng Asp 279(1–3):196–207

33. Garg VK, Kumar R, Gupta R (2004) Removal of malachite green dye from aqueous solution by adsorption using agro-industry waste: a case study of *Prosopis cineraria*. Dyes Pigm 62(1):1–10

34. Soubhagya AS, Moorthi A, Prabaharan M (2020) Preparation and characterization of chitosan/pectin/ZnO porous films for wound healing. Int J Biol Macromol 157:135–145

35. Motshekga SC, Ray SS, Onyango MS, Momba MN (2015) Preparation and antibacterial activity of chitosan-based nanocomposites containing bentonite-supported silver and zinc oxide nanoparticles for water disinfection. Appl Clay Sci 114:330–339

36. Sing KS (1985) Reporting physisorption data for gas/solid systems with special reference to the determination of surface area and porosity (Recommendations 1984). Pure Appl Chem 57(4):603–619

37. Jawad AH, Malek NNA, Abdulhameed AS, Razuan R (2020) Synthesis of magnetic chitosan-fly ash/Fe_3O_4 composite for adsorption of reactive orange 16 dye: optimization by Box-Behnken design. J Polym Environ 28(3):1068–1082

38. Mostafa MH, Elsawy MA, Darwish MS, Hussein LI, Abdaleem AH (2020) Microwave-assisted preparation of Chitosan/ZnO nanocomposite and its application in dye removal. Mater Chem Phys 248:122914

39. Wang H, Gong X, Miao Y, Guo X, Liu C, Fan YY, Li W (2019) Preparation and characterization of multilayer films composed of chitosan, sodium alginate and carboxymethyl chitosan-ZnO nanoparticles. Food Chem 283:397–403

40. Malek NNA, Jawad AH, Abdulhameed AS, Ismail K, Hameed BH (2020) New magnetic Schiff's base-chitosan-glyoxal/fly ash/Fe_3O_4 biocomposite for the removal of anionic azo dye: An optimized process. Int J Biol Macromol 146:530–539

41. Rao KM, Suneetha M, Park GT, Babu AG, Han SS (2020) Hemostatic, biocompatible, and antibacterial non-animal fungal mushroom-based carboxymethyl chitosan-ZnO nanocomposite for wound-healing applications. Int J Biol Macromol 155:71–80

42. Jawad AH, Abdulhameed AS (2020) Statistical modeling of methylene blue dye adsorption by high surface area mesoporous activated carbon from bamboo chip using KOH-assisted thermal activation. Energy Ecol Environ 5(6):456–469

43. Lingamdinne LP, Koduru JR, Chang YY (2018) Karri Process optimization and adsorption modeling of Pb (II) on nickel ferrite-reduced graphene oxide nano-composite. J Mol Liq 250:202–211

44. Jawad AH, Abdulhameed AS, Reghioua A, Yaseen ZM (2020) Zwitterion composite chitosan-epichlorohydrin/zeolite for adsorption of methylene blue and reactive red 120 dyes. Int J Biol Macromol 163:756–765

45. Ramlah AB, Jawad AH, Ishak MAM, Kasim NN (2018) $FeCl_3$-activated carbon developed from coconut leaves: characterization and application for methylene blue removal. Sains Malaysiana 47(3):603–610

46. Lagergren S (1898) Zur theorie der sogenannten adsorption geloster stoffe. Vet Akad Handl 24:1–39

47. Ho YS, McKay G (1998) Sorption of dye from aqueous solution by peat. Chem Eng J 70:115–124

48. Jawad AH, Mubarak NSA, Abdulhameed AS (2020) Hybrid crosslinked chitosan-epichlorohydrin/TiO_2 nanocomposite for reactive red 120 dye adsorption: kinetic, isotherm, thermodynamic, and mechanism study. J Polym Environ 28:624–637

49. Langmuir I (1918) The adsorption of gases on plane surfaces of glass, mica and platinum. J Am Chem Soc 40:1361–1403

50. Frenudlich HMF (1906) Over the adsorption in solution. J Phys Chem 57:385–471

51. Temkin MI (1940) Kinetics of ammonia synthesis on promoted iron catalysts. Acta Physiochim URSS 12:327–356

52. Rizzi V, Gubitosa J, Fini P, Romita R, Agostiano A, Nuzzo S, Cosma P (2020) Commercial bentonite clay as low-cost and recyclable "natural" adsorbent for the Carbendazim removal/recover from water: overview on the adsorption process and preliminary photodegradation considerations. Colloids Surf A Physicochem Eng Asp 602:125060

53. Ogunleye DT, Akpotu SO, Moodley B (2020) Adsorption of sulfamethoxazole and reactive blue 19 using graphene oxide modified with imidazolium based ionic liquid. Environ Technol Innov 17:100616

54. Vijayaraghavan K, Won SW, Yun YS (2009) Treatment of complex Remazol dye effluent using sawdust-and coal-based activated carbons. J Hazard Mater 167(1–3):790–796

55. Janaki V, Oh BT, Shanthi K, Lee KJ, Ramasamy AK, Kamala-Kannan S (2012) Polyaniline/chitosan composite: an eco-friendly polymer for enhanced removal of dyes from aqueous solution. Synth Met 162(11–12):974–980

56. Phan DN, Rebia RA, Saito Y, Kharaghani D, Khatri M, Tanaka T, Kim IS (2020) Zinc oxide nanoparticles attached to polyacrylonitrile nanofibers with hinokitiol as gluing agent for synergistic antibacterial activities and effective dye removal. J Ind Eng Chem 85:258–268

57. Nair V, Panigrahy A, Vinu R (2014) Development of novel chitosan–lignin composites for adsorption of dyes and metal ions from wastewater. Chem Eng J 254:491–502

58. Abbasi M (2017) Synthesis and characterization of magnetic nanocomposite of chitosan/SiO_2/carbon nanotubes and its application for dyes removal. J Clean Prod 145:105–113

59. Chinoune K, Bentaleb K, Bouberka Z, Nadim A, Maschke U (2016) Adsorption of reactive dyes from aqueous solution by dirty bentonite. Appl Clay Sci 123:64–75

60. Mate CJ, Mishra S (2020) Synthesis of borax cross-linked Jhingan gum hydrogel for remediation of Remazol Brilliant Blue R (RBBR) dye from water: adsorption isotherm, kinetic, thermodynamic and biodegradation studies. Int J Biol Macromol 151:677–690

61. Zafar MN, Dar Q, Nawaz F, Zafar MN, Iqbal M, Nazar MF (2019) Effective adsorptive removal of azo dyes over spherical ZnO nanoparticles. J Mater Res Technol 8(1):713–725

62. Zhang F, Chen X, Wu F, Ji Y (2016) High adsorption capability and selectivity of ZnO nanoparticles for dye removal. Colloids Surf A Physicochem Eng Asp 509:474–483

63. Jawad AH, Abdulhameed AS, Malek NNA, ALOthman ZA (2020) Statistical optimization and modeling for color removal and COD reduction of reactive blue 19 dye by mesoporous chitosan-epichlorohydrin/kaolin clay composite. Int J Biol Macromol 164:4218–4230